Palaeogeography, Palaeoclimatology, Palaeoecology 623 (2023) 111620

Contents lists available at ScienceDirect

Palaeogeography, Palaeoclimatology, Palaeoecology

journal homepage: www.elsevier.com/locate/palaeo

Revised magnetostratigraphy of the Linxia Basin in the northeast Tibetan Plateau, constrained by micromammalian fossils

Yan Zheng [a,*], Zhanxiang Qiu [a], Zhuding Qiu [a], Lu Li [a], Xiaohao Wei [b], Rui Zhang [b], Leping Yue [b], Tao Deng [a,*]

[a] Key Laboratory of Vertebrate Evolution and Human Origins, Institute of Vertebrate Paleontology and Paleoanthropology, Chinese Academy of Sciences, Beijing 100044, China

[b] Department of Geology, State Key Laboratory of Continental Dynamics, Institute of Cenozoic Geology and Environment, Northwest University, Xi'an, China

ARTICLE INFO

Editor: Dr. Howard Falcon-Lang

Keywords:
Magnetostratigraphy
Mammalian faunas
Oligocene
Miocene
Linxia Basin

ABSTRACT

The Linxia Basin along the northeastern margin of the Tibetan Plateau has drawn enormous attention due to its rich mammalian fossils and great potential for exploring regional tectonics, paleoenvironmental history, and bio-evolution. However, the geochronology of the sedimentary sequences is in great dispute owing to uncertain lithostratigraphic correlation and poorly calibrated magnetostratigraphy. From 2017 to 2021, we carried out lithostratigraphic correlation of the strata from the southern part of the basin, which is rich in fossils, to the Maogou section in the central basin, and established a solid intra-basinal lithostratigraphic framework with accurate fossil locations. Then, high-resolution magnetostratigraphic investigations were performed on the Maogou section, which comprises, from oldest to youngest, the Jiaozigou, Shangzhuang, Dongxiang, Liushu/Hujialiang, and "Liushu" formations. Magnetostratigraphic results show that the Maogou sedimentary sequence (from Jiaozigou to Liushu/Hujialiang formations) spans from chron C10r to chron C5r.2n, yielding an age of 29–11.6 Ma, with constraints from four mammalian assemblage levels. The revised magnetostratigraphy indicates that the Jiaozigou Formation corresponds to chrons C6Cn.3n–C10r (~23–29 Ma), with *Paraceratherium* fauna from the lower Jiaozigou Formation being determined as ~29 Ma, and that the Hujialiang Formation, containing *Platybelodon* fauna, corresponds to chrons C5r.2n–C5Ar.2r (~11.6–12.8 Ma). The revised magnetostratigraphy of the Maogou section has significantly refined the chronology of the Linxia Basin sedimentary sequences and its associated mammalian evolution, tectonism, and climate change in Central Asia.

1. Introduction

The Linxia Basin in the northeastern Tibetan Plateau is famous for its well-developed Cenozoic strata and rich mammalian fossil records. The geological survey, including lithostratigraphy and paleomagnetic analysis of the strata and fossils of the Linxia Basin, has been carried out in four stages since 1965 (Qiu et al., 2023b). Significant progress in detailed lithostratigraphic classification and paleomagnetic dating of the Linxia Basin has been made during the past decades (e.g., Li et al., 1995; Fang et al., 1995; Fang et al., 1997, 2003, 2016; Zhang et al., 2019). However, the ages assigned through initial magnetostratigraphic investigations were poorly determined, at least partly due to inaccurate allocations of some important mammalian fossils (Fang et al., 1995, 1997, 2003). Another potential anchor for the magnetostratigraphy was gypsum fission tracks (Chen et al., 1996), which led to underestimated ages due to the postdepostional origin of the gypsum. Since 2000, efforts by the Institute of Vertebrate Paleontology and Paleoanthropology (IVPP) to sequence lithostratigraphic units in terms of mammal fossils (Deng et al., 2004, 2013) have shown that the previously obtained paleomagnetic polarity units (Fang et al., 1997, 2003) were systematically correlated to much younger geomagnetic chrons. Moreover, the recently introduced Hujialiang Formation with its *Platybelodon* fauna in the southern part of the basin (Deng, 2004) was not included in previous work (Li et al., 1995; Fang et al., 1995). Therefore, clear stratigraphic sequences with precisely allocated mammal fossils are essential for elucidating the infilling process of the basin and the evolution of mammals.

Magnetostratigraphy calibrated by absolute ages or fossils is a useful geochronological method for providing age controls on sedimentary sequences (Opdyke and Channell, 1996). Several fossiliferous horizons

* Corresponding authors.
E-mail addresses: zhengyan@ivpp.ac.cn (Y. Zheng), dengtao@ivpp.ac.cn (T. Deng).

https://doi.org/10.1016/j.palaeo.2023.111620
Received 27 August 2022; Received in revised form 23 April 2023; Accepted 26 April 2023
Available online 9 May 2023

from the Linxia Basin can provide biochronologic constraints for magnetostratigraphy to establish a reliable chronological frame. From 2017 to 2021, our group conducted a basin-scale stratigraphic correlation from the southern to northern parts of the basin. Then, we performed a high-resolution magnetostratigraphic study on the Maogou section, representing one of the most continuous sedimentary sequences in the eastern part of the Linxia Basin. As a result, we obtained a revised magnetostratigraphy of the Maogou section, which was well constrained by four micromammal fossil assemblages. Our findings have provided new insights into the middle Cenozoic tectonosedimentary processes, paleoclimate, and biological evolution in the northeastern Tibetan Plateau.

2. Geological background

The uplift and outward expansion of the Tibetan Plateau is the most

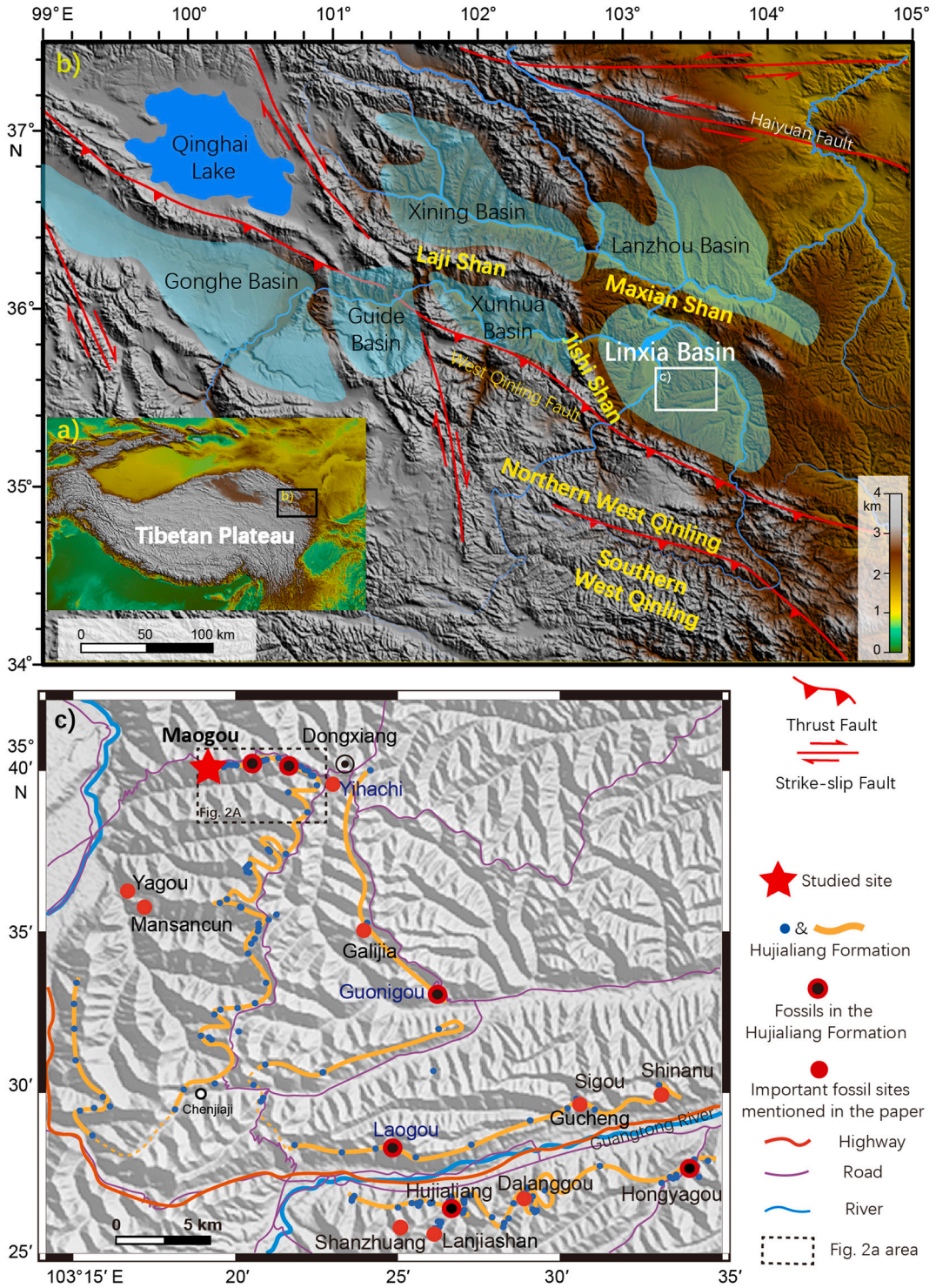

Fig. 1. Topography of the Tibetan Plateau (a) and basins and faults of orogenic belts at the northeast edge of the plateau (b) on the top (white rectangular marks the area of c); (c) locations of mammalian fossil sites (solid red circles and red circles filled with black) and distribution of Hujialiang Formation (light blue solid circles and yellowish-brown thick lines). (For interpretation of the references to colour in this figure legend, the reader is referred to the web version of this article.)

important geological event in the Cenozoic, significantly changing East Asia's topography and altering global climate circulation. Continual convergence of the Indian Plate with the Eurasian Plate developed thrust faults and folds on and around the Tibetan Plateau (e.g., van Hinsbergen et al., 2012). The constant northward push resulted in a series of structural thrust belts and basins forming around the northeast edge of the plateau (Fig. 1B), rendering it a key area to study basin-range coupling (e.g., Clark et al., 2010; Staisch et al., 2020). Deformation and exhumation of the east-west trending Laji Shan and Maxian Shan (Shan means mountain in Chinese), around 22 Ma (Lease et al., 2011), isolated the Linxia and Xunhua basins to the south of the Xining Basin. The uplift of Jishi Shan then separated the Xunhua and Linxia basins by approximately 13 Ma (Lease et al., 2011).

The Linxia Basin, one of the Cenozoic basins in the northeastern Tibetan Plateau (Fig. 1a), is famous for its well-developed strata and rich mammalian fossil records (see Fig. 1c). Qiu et al. (2023b) review the historical investigation of the Linxia Basin since 1965. Lithostratigraphic units in the northern part of the Linxia Basin (Maogou section) were re-classified to have a clear view of the sedimentary changes (Li et al., 1995; Fang et al., 1995) (Fig. 2; Table 1), which is a significant advance for the stratigraphy and sedimentology of the Linxia Basin. However, the magnetostratigraphic chronology was inaccurately assigned owing to the ambiguous allocation of fossils to rocks and uncertainties in the ages of gypsum fission tracks. Subsequently, biostratigraphic zonations were developed based on the precise correlation of the fossil localities with the formations in 2004 (Deng et al., 2004) and updated in 2013 (Deng et al., 2013). The controversy between previous magnetostratigraphy and biostratigraphy can be resolved by conducting the two aspects together. Recently, from 2017 to 2021, we performed detailed stratigraphic correlations from the southern part of the basin (with abundant fossil records) to the Maogou section (continuous sedimentary sequences) based on the sedimentological characteristics of the strata and fossil records (Figs. 1c and 2a). Then, we attempted to build a renewed magnetostratigraphic sequence based on stringent micromammal fossil assemblages.

3. Biostratigraphy of the Linxia Basin

Biostratigraphy of the Linxia Basin was built on numerous mammalian fossils (Deng et al., 2004, 2013). Seven important fossil sites (solid red circles in Fig. 1c) were selected to show crucial mammalian fossil layers and their lithostratigraphy (Fig. 3, Appendix Fig. 1). These micromammalian fossils were identified and classified by Qiu et al. (2023a).

3.1. Biostratigraphy at the seven crucial fossil sites

"Liushu" Formation comprises grayish-yellow clays interbedded with light yellowish-brown silty clays with carbonate nodules. Large collections of *Hipparion* fauna were excavated from this formation at many sites along the Guangtong River, such as Shanzhuang (LX200027) and Sigou (LX200007) (Fig. 3).

Hujialiang Formation is composed of grayish-yellow conglomerates and sandstones, yielding plenty of *Platybelodon* fauna fossils (Deng, 2004). This easily recognizable formation is sandwiched between the overlying "Liushu" Formation and the underlying Dongxiang Formation. A mandibular tusk of *Platybelodon* was found in the basal conglomerates of the Hujialiang Formation (Fig. 3e LX2017X, Appendix Fig. 3d-3). The *Platybelodon* fauna was also excavated from many other places, such as Shanzhuang (LX2000028), Hujialiang (LX200002), Laogou (LX200003), and Hongyagou (LX200017) (Fig. 3b). Micromammal fossils occur at Lanjiashan, Qijia, Duomusi, and Maogou (Qiu et al., 2023a) (Figs. 2 and 3).

Dongxiang Formation comprises reddish-brown clays/silty clays, frequently intercalated by striped green clay, the "zebra beds". The boundary of the Hujialiang and Dongxiang formations is clear (Appendix Figs. 1e-k and Appendix Fig. 3d-2). The presence of clay clasts (diameter > 50 cm) in the conglomerates implies considerable denudation in the upper parts of the Dongxiang Formation (Appendix Fig. 1c). Galijia (LX201705) and Shinanu (LX201501) (Fig. 3b and g) are two crucial Middle Miocene micromammal fossil sites. There are 27 genera and 37 species from 15 families and four orders at Galijia, six genera and seven species at Shinanu (Qiu et al., 2023a).

Shangzhuang Formation is composed of grayish-red silty clays. Micromammal fossils were found at two sites along the Guangtong River (Fig. 3e and f). There are 11 genera and 13 species belonging to seven families at the Gucheng fossil site (LX200051), six genera and six species belonging to four families at Dalanggou (LX201501) (Qiu et al., 2023a). These micromammal fossils suggest an age of Early Miocene for the Shangzhuang Formation. A 6.6 m thick gravel-sandstone layer at the base of the Dongxiang Formation at Dalanggou (Fig. 3e) has served as the boundary of the Dongxiang and Shangzhuang formations. However, thick vegetation cover makes it difficult to define the Dongxiang-Shangzhuang boundary at the Gucheng site (Appendix Fig. 3e).

Jiaozigou Formation comprises brownish-red silty clays rich in *Paraceratherium* fauna fossils from the central part of the basin (Yagou in Fig. 1) (Qiu et al., 2004; Deng et al., 2013). Micromammal fossils (LX200302) were found near the large mammal fossil site (LX200213) in Yagou (Wang and Qiu, 2023). There are 17 genera and 28 species belonging to 13 families at the Yagou fossil site; six genera and ten species in four families at Mansancun (Fig. 1) from the upper parts of the Jiaozigou Formation (Fig. 3a) (Wang et al., 2023; Qiu et al., 2023a).

3.2. Regional lithostratigraphic correlation

The conglomerate of the Hujialiang Formation can be prominently recognized due to their higher resistance to weathering and barren surfaces (Appendix Fig. 1 and 3). This newly named formation (Deng, 2004) bearing abundant fossils of *Platybelodon* fauna was not distinguished in the previous lithostratigraphy of the Linxia Basin (Fang et al., 1995). The Hujialiang Formation is recognizable along the Guangtong River, and abundant *Platybelodon* fossils were found in the sands and conglomerates (Fig. 1c). As such, we traced this formation from the south to the center of the basin to create a lithostratigraphic correlation (Fig. 1c and 2a). In the Dongxiang area, just above the Hujialiang Formation, *Hipparion* fauna was reported from the Yihachi site (Fig. 2) (Zhang et al., 2021). Conglomerates to the west lie unevenly over the Dongxiang Formation (Appendix Fig. 1 g-k). The conglomerates (Appendix Fig. 1i) of the Hujialiang Formation transition to cross-bedded coarse sandy layers (Appendix Fig. 1b) and horizontally bedded medium-grained sands (Appendix Fig. 1a) near Yangwa and finally into silts and silty clays west of the Maogou section. Micromammal fossils from Duomusi and Qijia resemble those of the Liushu Formation and the basal parts of the Hewangjia Formation at Maogou (dashed lines between Maogou and Yangwa East) (Fig. 2) (Qiu et al., 2023a). A *Platybelodon* tusk had been reported from the upper members of the Liushu Formation in the Maogou section (Fang et al., 1995). Given the precise dating of these mammal fossils, the Liushu Formation of Fang et al. (1995) would be equivalent to the Hujialiang Formation (Fig. 2) in the south of the basin. Based on this, we suggest that the "Liushu" Formation (with quotation marks) should be used for the strata containing *Hipparion* Fauna in the basin's southern part.

According to the systematic lithostratigraphic correlation, there was no noticeable significant lateral lithofacies change, contradictory to the previous reports concerning Guonigou. Fang et al. (2016) assigned yellowish-brown silty mudstone bearing various *Hipparion* and *Platybelodon* fossils to the Dongxiang Formation and the underlying "zebra bed" to Shangzhuang Formation. The misused formation names at Guonigou led to two perceived "zebra bed" sequences in the basin, and then "two phases of flexural deformation of the Linxia basin" wrongly concluded (Fang et al., 2016). In another magnetostratigraphic study at Laogou, an important *Platybelodon* site (Deng, 2004) was misallocated to the bottom

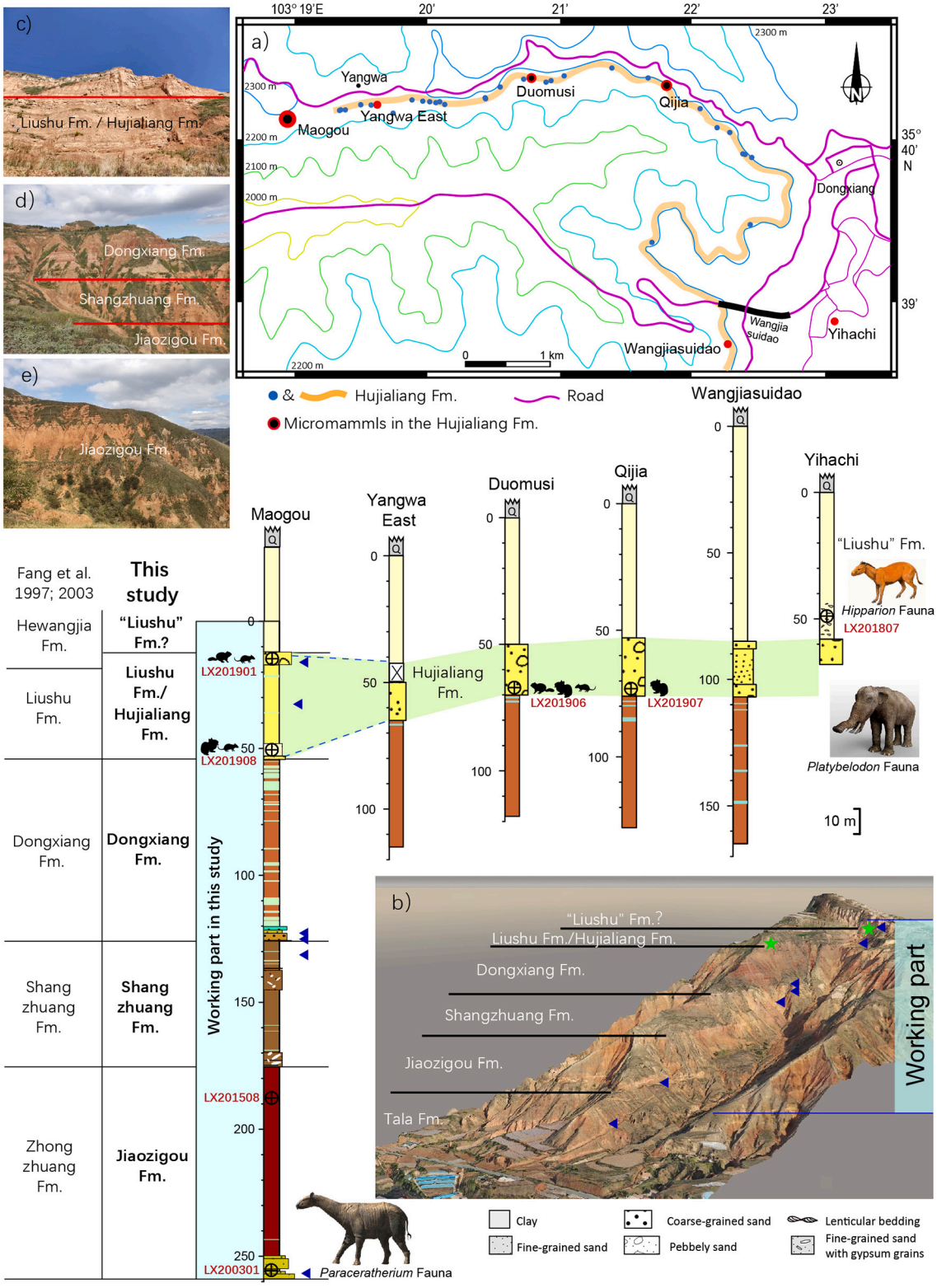

Fig. 2. A distribution of gravel-coarse sandy layers of the late Middle Miocene Hujialiang Formation in the Dongxiang area (thick yellow line in a) and regional stratigraphic comparisons of crucial sections (photographs are shown in Appendix Fig. 1). Light green belts on the lithological bars represent the greenish-gray clay in the Dongxiang Formation, measured at each layer in the Maogou section but without precise measurements in other sections. The micromammal fossils in Hujialiang Formation are shown as small sketch pictures beside lithology bars. The bottom two sites in the Jiaozigou Formation were excavated from the south valley (Fig. 1c, Mansancun and Yagou). An overview of the Maogou section by unmanned aerial vehicle below (green stars show the location of micromammals) (b). Photographs of the strata of the Maogou section (c-e). Blue triangles denote detrital zircon provenance analysis sites (He et al., 2023). (For interpretation of the references to colour in this figure legend, the reader is referred to the web version of this article.)

Table 1
Description of lithostratigraphic units in the Maogou section.

Fang et al., 1997, 2003	This study	Thickness (m)	Lithostratigraphic description and fossils	Fossil sites	Photo(s)
Hewangjia Fm.	"Liushu" Fm.?	~50	A massive, yellowish-brown clay/silty clay; paleomagnetic sampling through the lowest 12.1 m of the section		Fig. 2c
		5	Gray to yellowish-brown carbonate-cemented conglomerates (small gravel of 1–5 cm diameters) and coarse sand. Micromammal fossils: *Palaeosciurus* and *Plesiodipus*	Zhuan chang LX201901	Appendix Fig. 2a
Liushu Fm.	Liushu Fm./ Hujialiang Fm.	31	Yellowish-brown mudstones interbedded with medium- and thin-bedded light yellow-brown silty clay, with carbonate nodules		Fig. 2c
		5	Yellowish-brown silt		
		1.3	Yellowish-brown fine sand. Micromammals: *Alloptox* and *Sayimys*	Yangwa LX201908	
		66	Reddish-brown mudstones interbedded with medium- and thin-bedded white or greenish-gray clay		Fig. 2d
Dong-xiang Fm.	Dong- xiang Fm.	5.5	Colorful coarse-medium sand		Appendix Fig. 2b-c
		0.5	Gray conglomerate (gravel diameter < 1 cm)		Appendix Fig. 2d
		10.7	Yellowish-brown mudstones		Fig. 2d
Shang- zhuang Fm.	Shang- zhuang Fm.	8.6	Yellowish-brown silt with primary and secondary gypsum		Appendix Fig. 2e
		24.7	Yellowish-brown mudstones and silt		
		5	Yellowish-brown silt with primary and secondary gypsum		
Zhong- zhuang Fm.	Jiaozigou Fm.	74.5	Reddish-brown clay/silty clay. Micromammal fossils: 6 genera and 10 species in 4 families	Mansan cun LX201508	Fig. 2e
		8.9	Light yellow sand and conglomerate. *Paraceratherium* Fauna. Micromammal fossils: 17 genera and 28 species in 13 families	Yagou LX200301	Appendix Fig. 2f-g
Tala Fm.	Tala Fm.	~50	Reddish silt-sandstone, mostly covered by vegetation		Appendix Fig. 2 h

The micromammalian fossils of Zhuanchang and Yangwa were excavated from the Maogou section.

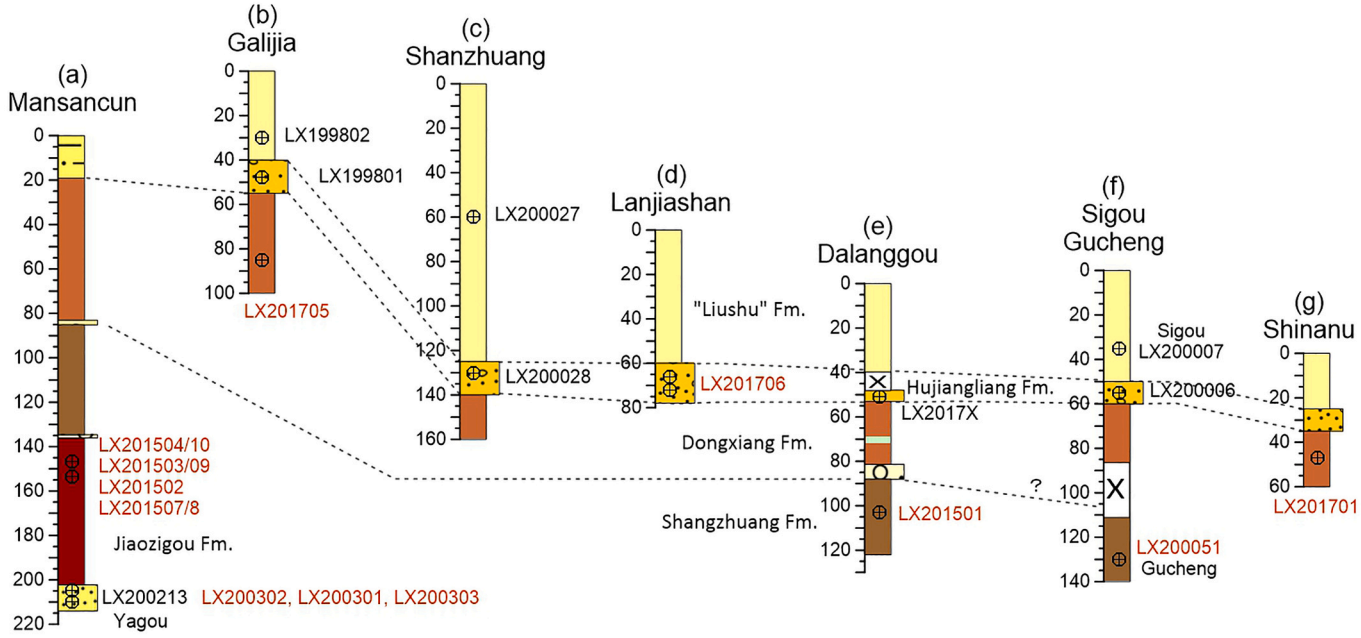

Fig. 3. Lithostratigraphic horizons of crucial mammalian fossil sites (a-g) (circle with a cross inside represents the fossil position with fossil site numbers. Black numbers for large mammals (most of these fossils were introduced in Deng et al., 2013), and red characters indicate micromammalian sites (Qiu et al., 2023a; Wang and Qiu, 2023; Wang et al., 2023). Photographs and section details of Yagou-Mansancun (a) were shown in Wang and Qiu (2023) and Wang et al. (2023). Photographs six fossil sites (b-g) shown in Appendix Fig. 3. A mandibular tusk of *Platybelodon* (LX2017X) was found at Dalanggou during stratigraphic correlations in 2017 (Appendix Fig. 3d-3). (For interpretation of the references to colour in this figure legend, the reader is referred to the web version of this article.)

of the Dongxiang Formation (Zhang et al., 2019). In these cases, magnetostratigraphic correlations followed the mammal ages indicated by paleontologists, but formation names were inaccurately used and led to an incorrect chronology of the strata and mistaken conclusions (Fang et al., 2016; Zhang et al., 2019). In this study, we clarify Linxia Basin lithostratigraphy through systematical lithostratigraphic correlations from the south to the center of the basin and then build reliable magnetostratigraphy with precise fossil records.

4. Sampling and methods

4.1. Sampling

A composite lithostratigraphy was built based on data from various locations in the basin and typified by the Maogou section (Fang et al., 1995, 1997, 2003). We described the lithology of the measured section (Table 1), similar to the previous composite but differing in thickness (Fig. 2 and Table 1). In 2020, 718 paleomagnetic samples were collected at 20 cm and 50 cm intervals from a 259 m thick sediment sequence of the Maogou section (Fig. 2), and 666 samples were measured. Unoriented samples were also collected at 20-cm intervals for other analyses.

4.2. X-ray diffraction (XRD) analyses

Representative samples were collected from each formation for mineral analysis, and two samples represent greenish-gray clay and reddish-brown clay/silt, respectively, from the Dongxiang Formation. Samples were ground into powder and pressed on a glass holder. The mineral components were identified using a Rigaku MiniFlex II Desktop X-ray diffractometer with Cu Kα ($\lambda = 1.5406$ Å) radiation. The experimental conditions were as follows: voltage of 30 kV, current of 15 mA, divergence slit of 1.25°, an anti-scattering slit of 1.25°, and receiving slit width of 0.3 m. Samples were scanned over an angular 2θ range from 10 to 75° with a 1°/min scanning speed. These measurements were conducted at the Key Laboratory of Vertebrate Evolution and Human Origins, the Institute of Vertebrate Paleontology and Paleoanthropology, Chinese Academy of Sciences.

4.3. Rock magnetic measurements

Representative subsamples from each formation were selected for detailed magnetic mineral analyses. Powdered subsamples filled in the cubic ceramic box were subjected to stepwise thermal demagnetization experiments (Lowrie, 1990) after applying direct fields of 2.5, 0.5, and 0.1 T, respectively, along three mutually perpendicular axes of the cubic boxes. Measurements were performed by a 2-G Enterprises pulse magnetizer, followed by thermal demagnetization in 18 steps from room temperature to 690 °C (100 °C, 200 °C, 300 °C, 350 °C, 400 °C, 450 °C, 500 °C, 525 °C, 550 °C, 575 °C, 585 °C, 600 °C, 620 °C, 640 °C, 660 °C, 680 °C, and 690 °C).

The magnetic hysteresis parameters and first-order reversal curve (FORC) diagrams were measured using a vibrating sample magnetometer (VSM 3900), Princeton Measurements Corporation. Approximately 800 mg of the subsamples were stored in capsules for measurement. First, isothermal remanence (IRM) acquisition (1.5 T) (in logarithmic increments) and back-field demagnetization curves were measured, from which the coercivity of remanence (H_{cr}) was obtained. Then, hysteresis parameters, saturation magnetization (M_s), saturation remanence (M_r), and coercive force (H_c) were determined from the hysteresis loops (maximum applied field of 1 T) after subtracting the high-field contributions. Finally, we obtained first-order reversal curve (FORC) (Roberts et al., 2000) measurements, 120 curves with a field increment of 2.07 mT, averaging time of 500 ms, and a 1 T saturating field. The FORC distributions were calculated using the FORCinel package (Harrison and Feinberg, 2008) with an optimum smoothing factor (SF) of 5. Remanence and other magnetic measurements were conducted at the Paleomagnetism and Geochronology Lab (PGL) of the Institute of Geology and Geophysics, Chinese Academy of Sciences, Beijing.

4.4. Paleomagnetic measurements

Anisotropy of magnetic susceptibility (AMS) was measured for oriented samples in a 200 A/m alternating field using an MFK-FA Kappabridge magnetic susceptibility meter (AGICO, sensitivity 2×10^{-8} SI). We also measured the susceptibility of unoriented samples kept in a non-magnetic plastic cubic box. The two measurements were performed at the Paleomagnetism and Environmental Magnetism Laboratory of the China University of Geosciences in Beijing (CUGB). Subsequently, we performed stepwise thermal demagnetization of natural remanent magnetization (NRM) on oriented cubic samples using a PGL-100 thermal demagnetizer by Qin et al. (2020) by 24 steps from room temperature to 690 °C (80 °C, 150 °C, 200 °C, 250 °C, 300 °C, 350 °C, 400 °C, 450 °C, 475 °C, 500 °C, 525 °C, 550 °C, 575 °C, 585 °C, 610 °C, 620 °C, 630 °C, 640 °C, 650 °C, 660 °C, 670 °C, 680 °C, and 690 °C). After each step, the remaining remanences measurements were performed in a magnetically shielded room using 2-G Enterprises pass-through cryogenic magnetometers equipped with high-resolution pick-up coils with a noise level of 10^{-6} A/m. Finally, principal component analyses were carried out on the paleomagnetic results to obtain characteristic remanent magnetization (ChRM) using the PuffinPlot program (Lurcock and Wilson, 2012).

5. Results

5.1. Mineral compositions

5.1.1. XRD results

The X-ray diffraction peaks identified four significant minerals in the sediments: quartz, carbonate, gypsum, and dolomite (Fig. 4a-f). Four samples (from the "Liushu", Liushu/Hujialiang, reddish-brown clay in the Dongxiang, and Jiaozigou formations) have similar mineral compositions, with quartz and calcium carbonate being the dominant minerals. The greenish-gray clays in the Dongxiang Formation are dominated by dolomite, resulting in the light colorization of the sediment. The Shangzhuang Formation contains quartz, dolomite, and gypsum. The large gypsum sheets can be observed in the sediments (Appendix Fig. 2e).

5.1.2. Three-axis thermal demagnetization

High (2.5–0.5 T), medium (0.5–0.1 T), and low coercivity (<0.1 T) magnetic components gradually demagnetized during the heating process. The three components of the greenish-gray clay (Fig. 4i) almost entirely demagnetized at 575 °C, the unblocking temperature of magnetite. Magnetizations of this sample were much lower than those of other samples, indicating a low concentration of magnetic minerals. The low concentration of magnetite dominated the magnetic signals of the greenish-gray clays. The low coercivity components of the other five samples displayed unblocking temperatures of 640–680 °C, higher than the magnetite Curie temperature, indicating that the low coercivity component is still affected by high coercivity components. Medium and high coercivity components exhibit similar demagnetization behavior, with unblocking hematite temperatures of 680 °C (Fig. 4g-l). We thus concluded that the dominant magnetic minerals in the Linxia Basin were hematite and magnetite.

5.1.3. Hysteresis loops

The magnetic signals from greenish-gray clays of the Dongxiang Formation were too weak to obtain reliable hysteresis-related measurements, so five samples from the five formations were measured (Fig. 5). Wasp-waist-shaped hysteresis loops (Fig. 5a-e) indicate both high and low coercivity magnetic minerals in the samples. Hysteresis parameter ratios, M_r/M_s were similar in the five results, but H_{cr}/H_c values for the Dongxiang and Jiaozigou formations were higher than those in the other three formations. This difference might be related to high values of H_{cr} (Figs. 5c and e), suggesting more significant quantities of hematite in the two formations.

5.1.4. IRM acquisition curves

Decomposed fractions from IRM acquisition curves can discriminate components with different magnetic properties (e.g., Heslop et al., 2002). Three groups were recognized: component 1 with a $B_{1/2}$ of 31–36

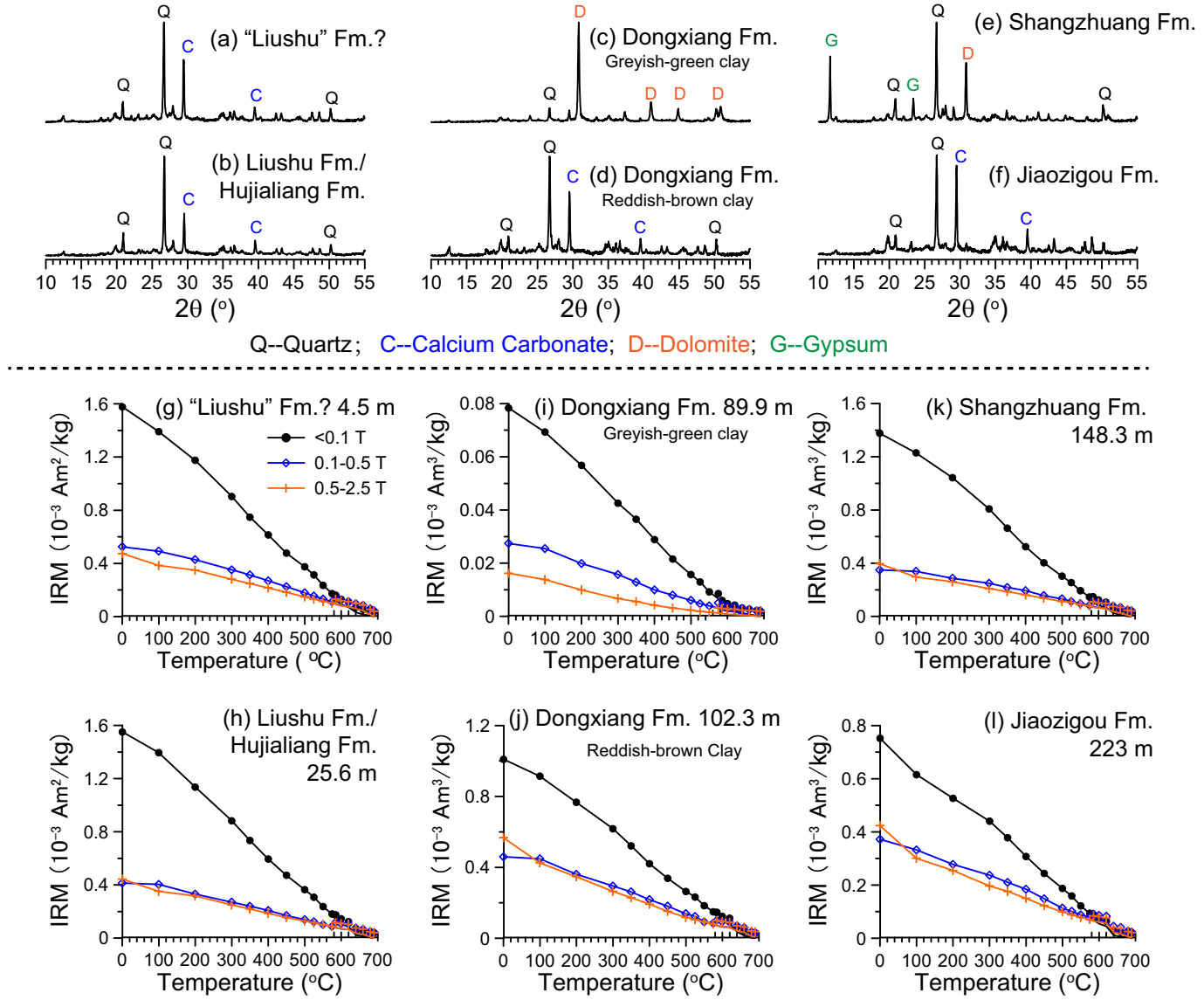

Fig. 4. Mineral compositions of each formation: XRD patterns (10–55°) (C-calcium carbonate; D-dolomite; G-gypsum; Q-quartz) (a-f) and three-axis thermal demagnetizations (g-l). Two representative samples (greenish-gray and reddish-brown clay) shown for the Dongxiang Formation. (For interpretation of the references to colour in this figure legend, the reader is referred to the web version of this article.)

mT, component 2 with a $B_{1/2}$ of ~300 mT, and component 3 with a $B_{1/2}$ of ~5 mT (Fig. 5f-j and Table 2). Component 1 had a relatively constant mean coercivity and was found to be the significant magnetic carrier for the "Liushu", Liushu/Hujialiang, and Shangzhuang formations. Component 2 was characterized by high coercivity and was reportedly higher in the Dongxiang (reddish-brown clays) and Jiaozigou formations, with also a high H_{cr} (Fig. 5c and e). The results indicate higher quantities of hematite in the Dongxiang and Jiaozigou formations. Component 3 had a low coercivity and contributed ~5% to the bulk SIRM, thus representing magnetite.

5.1.5. *FORC diagrams*

We used the FORC distribution to recognize the magnetic domains and assess the magnetic mineralogy of these natural samples (e.g., Roberts et al., 2000; Egli et al., 2010). Fig. 5 k-o shows a central ridge signature associated with moderate vertical spreading along the Hu axis at low coercivities, demonstrating a dominantly single domain (SD) magnetite signature with weak to moderate interactions.

Quartz, carbonate, gypsum, and dolomites formed the primary mineral composition of the Linxia Basin. Dolomite dominated the greenish-gray clays of the Dongxiang Formation, whereas gypsum only existed in the Shangzhuang Formation. Since hematite and SD magnetite were the primary magnetic minerals in the basin, we applied thermal demagnetization to obtain paleomagnetic results.

5.2. *Susceptibility*

Bulk susceptibility and AMS mean susceptibility values displayed slight increment from the bottom to the top of the Jiaozigou Formation and maintained high values for the Shangzhuang Formation (~20 × 10^{-8} m^3/kg) with minor fluctuations (Fig. 6a). Susceptibility in the Dongxiang and Hujialiang formations were found to have a significant relation to lithology, with lower values correlating to greenish-gray clays. The susceptibility in the "Liushu" Formation was approximately 10–20 × 10^{-8} m^3/kg.

5.3. *AMS*

The orientations of the AMS axes usually have structural significance (e.g., Jelinek, 1981; Borradaile and Jackson, 2010), widely applied in

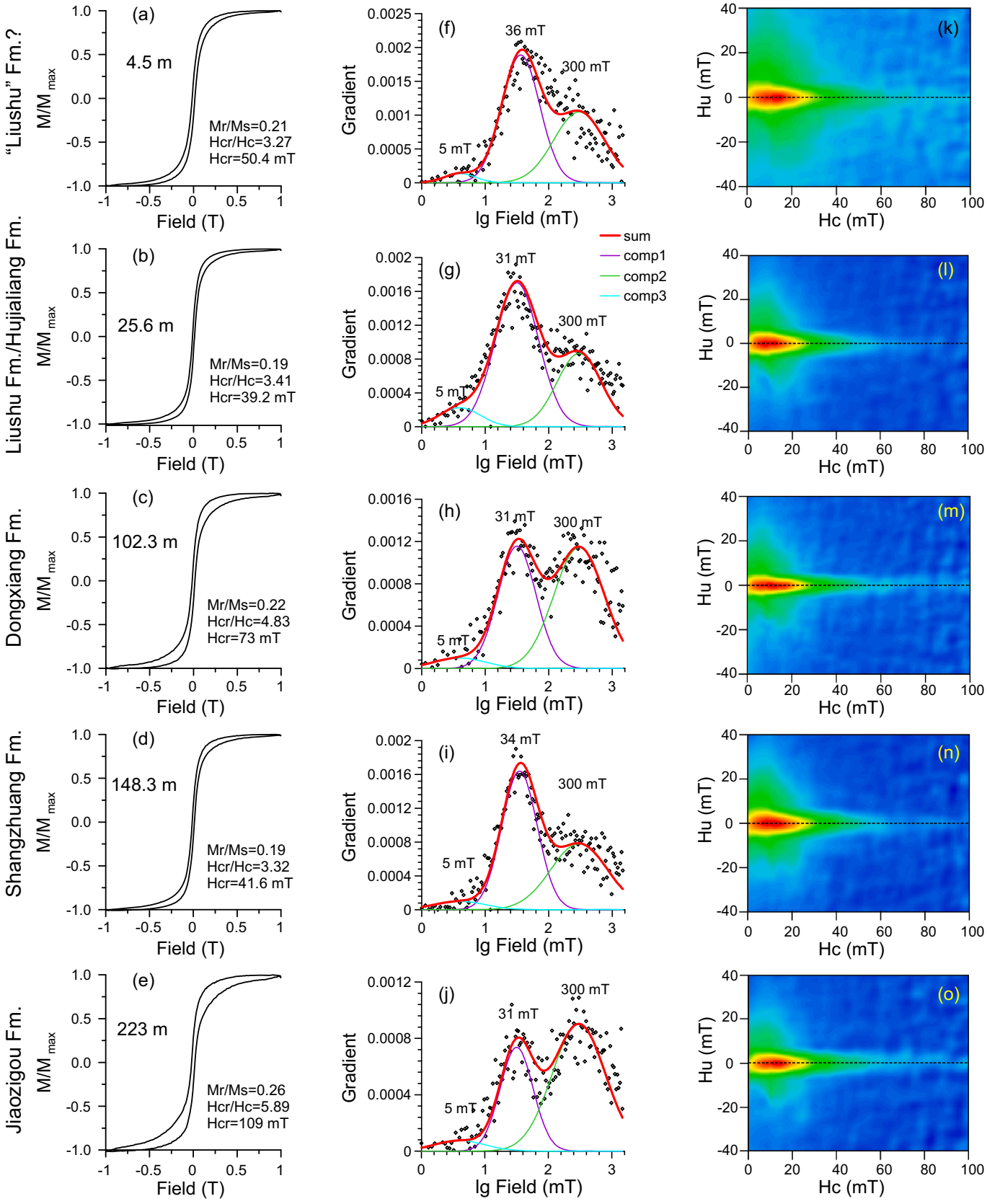

Fig. 5. Hysteresis loops (a-e), IRM acquisition curves (f-j), and FORC diagrams (k-o) (smooth factor is 5) of each formation.

Table 2
Magnetic component information from IRM acquisition curves.

	Component 1 $B_{1/2}$:31–36 mT	Component 2 $B_{1/2}$: ~300 mT	Component 3 $B_{1/2}$: ~ 5 mT
"Liushu" Fm.?	**56%**	41%	3%
Liushu/Hujialiang Fm.	**61%**	32%	7%
Dongxiang Fm.	41%	**54%**	5%
Shangzhuang Fm.	**54%**	41%	5%
Jiaozigou Fm.	32%	**63%**	5%

numerous tectonic studies (e.g., Li et al., 2020; Xiao et al., 2021; Jiang et al., 2022). The magnitude ellipsoid of the AMS is described by three principal susceptibilities (κ_{max}, κ_{int}, κ_{min}). We measured 666 samples, but 24 exhibited different behaviors, resulting in poor demagnetization results. Therefore, only 642 results were used for analyses (Fig. 6c). κ_{max} axes were distributed horizontally around the edge of a stereographic projection, while κ_{min} axes displayed a vertical upright orientation (Fig. 6). κ_{max} and κ_{min} have been shown for each formation to obtain a clear understanding of the AMS distribution. In the Jiaozigou Formation, κ_{max} axes were mainly distributed in the northwest and southeast, indicating slight stress along the southeast and northwest. However, the distribution on the two sides was unclear in the Shangzhuang Formation. The AMS results reflect horizontal depositional features from the Dongxiang Formation to the top.

5.4. Paleomagnetic results

Representative demagnetization behavior for each formation has been shown in Figs. 6d and e. Demagnetization comprises two to four magnetic components. Viscous remanence was removed by thermal demagnetization at 200–300 °C (Fig. 6d). A high-stability ChRM component was recognized between 580 and 680 °C, indicating the remanence carrier to be hematite. The maximum angular deviation (MAD) was <15° (80% of the results were < 10°) (Fig. 7d). A total of 558 (83.7%) samples provided reliable ChRM directions.

Virtual geomagnetic pole (VGP) latitudes were determined from the ChRM vector directions and subsequently used to define the magnetic polarities (Fig. 7e). Reversal tests were performed on samples with VGP latitudes higher than 45° or less than −45°. The mean normal direction was calculated to be $D/I = 6/48.6°$ ($a_{95} = 2.85°$, $n = 199$), while the mean reversal was $D/I = 184/-41.1°$ ($a_{95} = 2.53°$, $n = 262$). The angular difference between the two directions was 7.6°, a nearly antipodal character, suggesting a primary ChRM. Sixteen major reverse chrons and fifteen major normal chrons were identified, along with some small events (Fig. 7f).

6. Discussion

6.1. Revised magnetostratigraphy constrained by fossils

In this study, we performed stratigraphic correlation from the south to the center of the basin (Fig. 1c and 2a) and tracked the stratigraphic distribution of the mammalian fossils in the basin (Fig. 2 and 3). Based on the stratigraphic foundation, the biostratigraphy of the Linxia Basin is the same as that of Deng et al. (2013), with newly reported micromammalian fossil assemblages (Qiu et al., 2023a): the Tala (non-fossiliferous), Jiaozigou (*Paraceratherium* fauna), Shangzhuang (Gucheng and Dalanggou assemblages), Dongxiang (Shinanu, Galijia, and Gucheng assemblages), Hujialiang (*Platybelodon* fauna), and "Liushu" formations (*Hipparion* fauna) (Fig. 3).

To resolve correlation of magnetostratigraphy to the GPTS, we carried out high-resolution paleomagnetic sampling in the Maogou section (20 cm or 50 cm intervals compared to the earlier 1 m intervals of Fang et al., 1997, 2003). Our paleomagnetic results showed a stable demagnetization behavior (Fig. 6d), providing reliable high-resolution results. The revised magnetostratigraphy showed similar paleomagnetic polarity patterns over the long term compared to previous findings (Fig. 8c and d), indicating great similarity in the two paleomagnetic works of over 25 years. However, the assigned ages differed since the previous magnetostratigraphy was constrained by fossils from other areas in the basin without clear lithostratigraphic correlations. The inaccurate allocation of mammal fossils to the Maogou lithostratigraphy resulted in younger ages at that time. Four fossil sites in the basin (No. 3, 5, 6, and 7) cited by Fang et al. (2003) were correlated to Liushu, Dongxiang, Shangzhuang, and Zhongzhuang formations of the Maogou section, respectively (Fig. 8), but fossil records were ambiguous at that time. Firstly, giant rhinos (fossil site 7 beside Fig. 8f) found in basal Jiaozigou Formation were supposedly Early Miocene (Qiu et al., 1990), but the age was revised as Late Oligocene in 2004 (Qiu et al., 2004). The mistake is due to a Miocene *Gomphotherium* tusk fossil mixed in with Oligocene mammal fossils (Deng et al., 2004). Secondly, Fang et al. (2003) correlated the fossils from Shanzhuang (fossil site 6 beside Fig. 8f; note spelling) with the Shangzhuang Formation. Late Miocene *Hipparion* and Middle Miocene *Platybelodon* fossils at the Shanzhuang section were excavated from two fossil layers (LX200027 and LX200028 in Fig. 3c). The mixed fossils were incorrectly correlated to the Shangzhuang Formation in the Maogou section (Fang et al., 2003). Thirdly, fossil sites 3 and 5 (Fang et al., 2003) bearing Late Miocene Hipparion were mistakenly correlated to the Liushu and Dongxiang formations, respectively (Fig. 8f). These fossils were matched inappropriately to strata in previous magnetostratigraphy. Fang et al. (1997, 2003) also applied age estimates for the Maogou section, which were derived from gypsum fission tracks of mainly postdepostional gypsum grains or sheets (Appendix Fig. 2e), and therefore too young. Overall, the previous magnetostratigraphy by Fang et al. (1995, 1997, 2003) was thus correlated to younger ages than expected. Here, we present stringent constraints on the proposed revised magnetostratigraphy (Fig. 7) by accurate micromammalian fossil records (Qiu et al., 2023a).

Paraceratherium fauna is typical for the Jiaozigou Formation, yielding a Late Oligocene age (Qiu et al., 2004). Nearby micromammal fossils (LX200302), excavated beside the large mammal site (LX200213) at the basal part of the Jiaozigou Formation in Yagou (Fig. 3a), include some primitive forms of the ULT III biozone and biozone C and some advanced genera like those in ULT II biozone and biozone B (early and late Oligocene biozones; see Wang and Qiu, 2023). Thus, the Yagou assemblage represents a fauna between the Early and Late Oligocene, as represented in China and Mongolia (Wang and Qiu, 2023). Another micromammal fossil assemblage from the upper parts of the Jiaozigou Formation in Mansancun (Fig. 3a; Wang et al., 2023) is Late Oligocene in age, so the Jiaozigou Formation is mainly Oligocene. The paleomagnetic chron correlations for this formation would be R12 equals the long reversal chron C6Cr, and N11 is C6Cn.2n-3n. N12 and R13 match C7, and N13-R16 correlate with C8 to C10 of the GPTS. There is no sample from the sands and conglomerates at the bottom part of the Jiaozigou Formation (Appendix Fig. 2f and g). We estimate the basal sand-conglomerates of the Jiaozigou formation to represent chron C10r or C11n. In this case, polarity chrons from the Jiaozigou Formation would be correlated with C6Cn.2n to C10r (23–29.18 Ma) in the GPTS (Fig. 7). Yagou assemblage is projected to ~29 Ma, and Mansancun assemblage would be approximately 24–25 Ma.

Micromammal fossils in the Shangzhuang Formation have been excavated from Dalanggou (LX201501) and Gucheng (LX200051) along the Guangtong River, yielding an Early Miocene age (Figs. 3e and f). Three minimum detrital zircon ages of approximately 16.8–17.4 Ma, at the bottom of the Dongxiang Formation and the upper parts of the Shangzhuang Formation (He et al., 2023) (Fig. 7), indicate a continuous sedimentary sequence between the two formations and provide a constraint age of upper Shangzhuang Formation, ~ 17 Ma. The magnetic polarity chrons N8-R11 do not correspond well with the GPTS during the Early Miocene. The revised paleomagnetic results are similar to the previous data (Fig. 8c and d) and another study from the southern valley

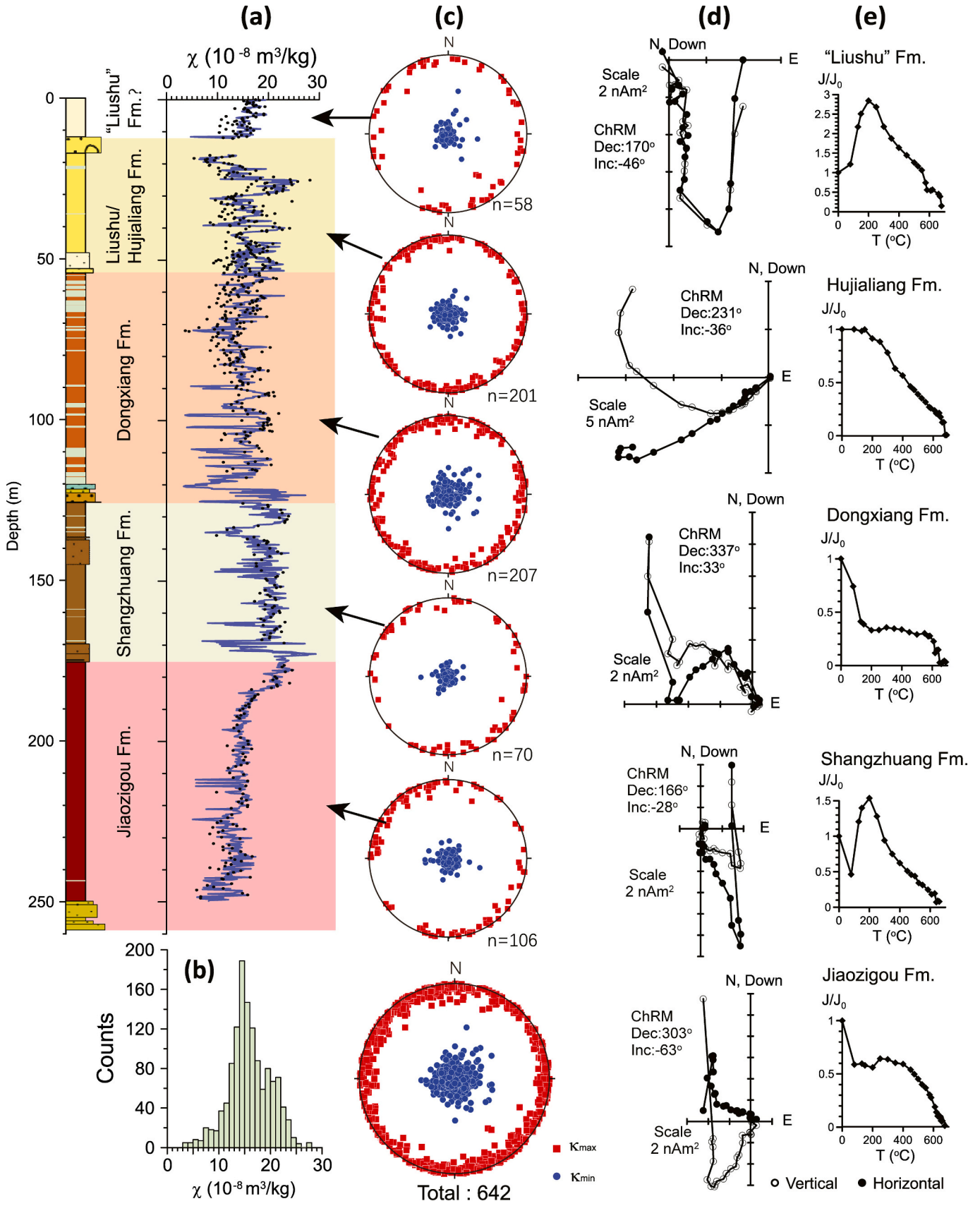

Fig. 6. Variation of susceptibility (AMS mean susceptibility in black dots and unoriented crushed samples in blue) (a), histogram of susceptibility (b), stereographic projections of AMS (c) (κ_{max} in red squares and κ_{min} in blue dots), vector end-point diagrams of NRM demagnetization (d) normalized decay curves on representative samples (e) (open and solid circles represent NRM projections onto vertical and horizontal planes, respectively). (For interpretation of the references to colour in this figure legend, the reader is referred to the web version of this article.)

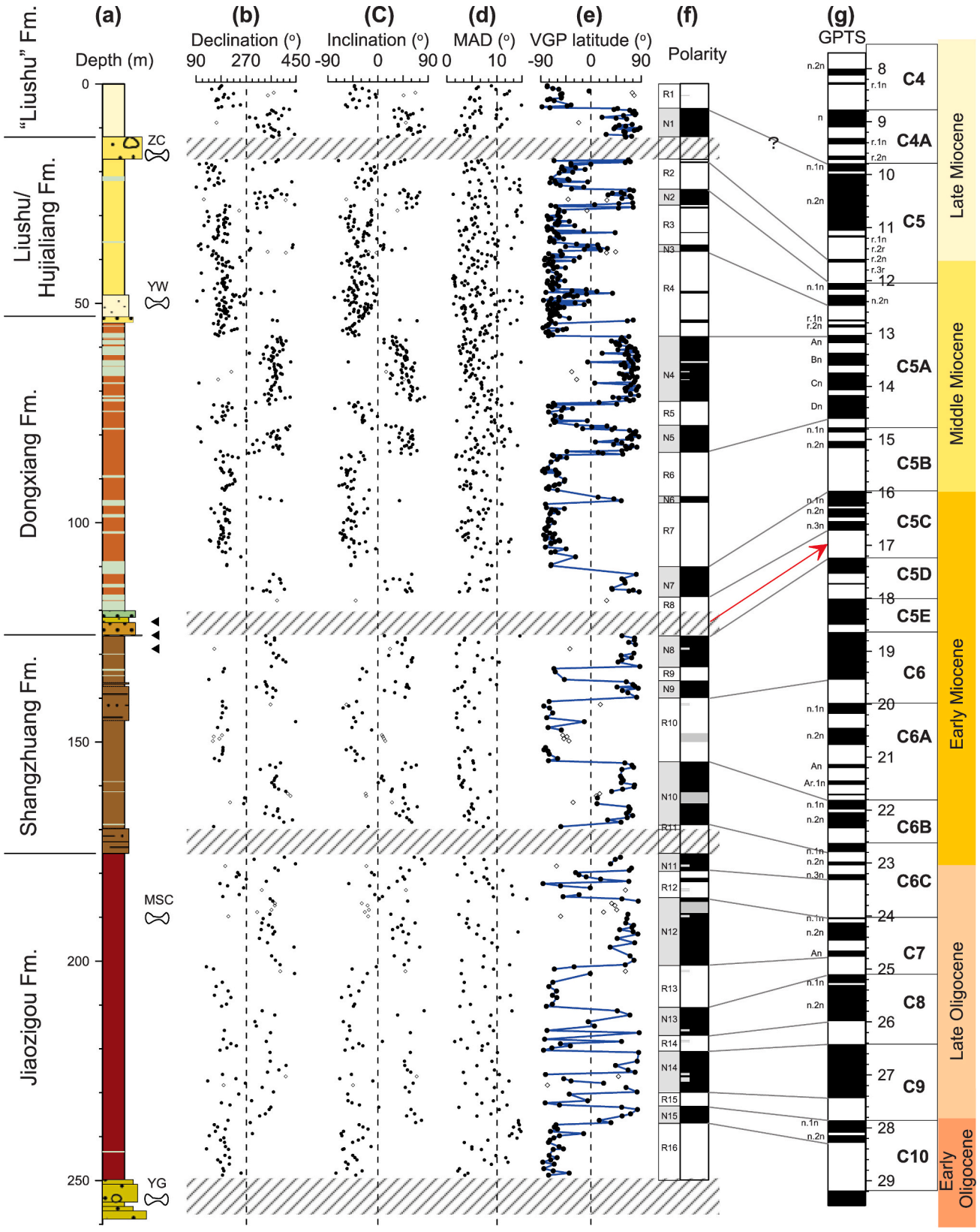

Fig. 7. Magnetic polarity stratigraphy of the Maogou profile: lithostratigraphy (a); declination (b); inclination (c); maximum angular deviation (MAD) (d); virtual geomagnetic pole (VGP) latitude (e); magnetic polarity zonation (f); geomagnetic polarity timescale (GPTS) (Ogg, 2020) (g). Four fossiliferous horizons beside (a) from top to bottom: Zhuanchang-ZC; Yangwa-YW; Manshancun-MSC; Yagou-YG. Solid circles represent reliable ChRM, while diamonds resemble mismatched inclination/declination results (light gray bars in f). One abnormal polarity result was also marked as a small gray bar in f. Three black triangles beside lithostratigraphy represent the sampling locations for detrital zircon analysis.

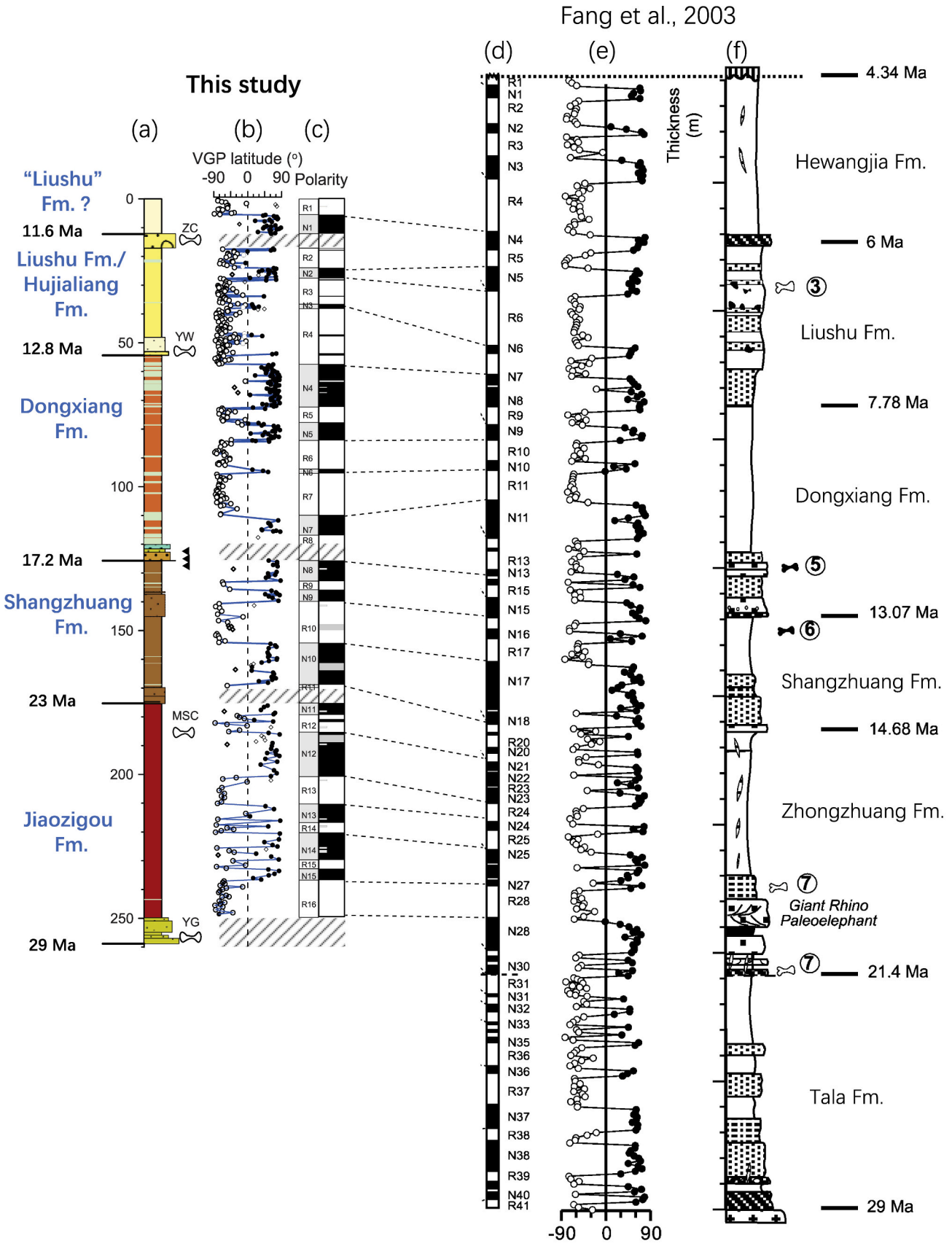

Fig. 8. Comparisons of lithostratigraphy, VGP, and polarity of this study (a-c) to previous results (d-f) (Fang et al., 2003). Four micromammalian fossil layers constrained our revised magnetostratigraphy: the upper two fossil layers (ZC and YW) were excavated from the Maogou section, and the bottom two (MSC and YG) were from nearby (Fig. 1C and Fig. 3a). Fossils in Fang's results (2003) are far from the paleomagnetic section without clear stratigraphic correlations.

of Maogou (Mansancun-Niujiacun section) (Sun et al., 2023), which is possibly like that of the basin. We correlate the strikingly long reversed interval R10 with the long predominantly reversed chrons in C6A. The short polarity chrons in C6A are missing in our observed polarity sequences due to large sampling intervals and the low sedimentation rate in this formation. Next, the long normal interval N8-N9 with short reverse chron R9 match C5D–C6n. N10 was compared with C6B–C6Cn.1n, and the small reversal chron R11 with C6Cn.1r. Deposition of the Shangzhuang Formation was estimated between 23 and 17.2 Ma.

Micromammal fossils in the Dongxiang Formation have been excavated from Galijia (LX201705) and Shinanu (LX201701), yielding a Middle Miocene age (Qiu et al., 2023a) (Figs. 3b and g). The Dongxiang Formation contains four normal-polarity zones and four reversed zones (N4-R8). The minimum detrital zircon ages of sand-conglomerate at the bottom of the Dongxiang Formation is ~17 Ma (He et al., 2023) (Fig. 7), so we correlated the bottom two chrons (N7 and R8) in the Dongxiang Formation with C5C (Fig. 7). The thick greenish-gray sediments here hinder detection of small reversal subchrons in C5C. The significant long reversed polarity chrons R6 and R7 with a short normal interval N6 are correlated with the long predominantly reversed polarity C5B. Then, the long normal polarity chrons N4 and N5 with a small reversal chron R5 corresponded to C5AAn-Dn. The long normal polarity zone with a few reversals in N4 does not perfectly match C5AAn-Cn, which may be related to the low deposition rate of greenish-gray sediments. The boundary between Dongxiang and Liushu/Hujialiang Formation is a short normal interval in R4, correlated with C5Ar.2n, indicating a boundary age of 12.8 Ma. Therefore, Dongxiang Formation was deposited during 17.2–12.8 Ma.

The Hujialiang Formation is coarse sand-conglomerate layers along the Guangtong River (Appendix Fig. 3). The conglomerates of the Hujialiang Formation transition to cross-bedded coarse sandy layers (Appendix Fig. 1b) to horizontally bedded medium-grained sands (Appendix Fig. 1a) near Yangwa, and finally into silts and silty clays westward of the Maogou section. Micromammal fossils in the Hujialiang Formation excavated from Lanjiashan (Fig. 3d, LX201706), Duomusi (Fig. 2, LX201906), Qijia (Fig. 2, LX201907) resemble those of the Yangwa (201908) and Zhuanchang (201901) at Maogou (Fig. 2) (Qiu et al., 2023a), yielding a late Middle Miocene age. The fossil (*Sayimys* sp. nov. and *Alloptox* sp.) at Yangwa in the fine sandy layers (53.1–54.4 m in R4) at the bottom of Liushu/Hujialiang Formation (Fig. 2 and 7) would date to ~12.8 Ma. Fossils at Zhuanchang (*Palaeosciurus* sp. and *Plesiodipus leei*) belonged to the conglomerate (~12–17 m between N1 and R2) (Fig. 2 and 7) would date similarly to the late Middle Miocene (Qiu et al., 2023a). The predominantly reversed polarity chrons in the Liushu/Hujialiang Formation should be correlated with C5r-C5Ar, also reported at Laogou (Fig. 1) along the Guangtong River (Zhang et al., 2019). The Zhuanchang fossils above a short normal interval above R2 match C5r.2n, which provides an age of 11.6 Ma for Zhuanchang micromammal fossils. N2-N3 had to be correlated with C5An. The two small normal polarity zones in R4 were correlated to C5Ar.1n and C5Ar.2n. Consistent with these results, the lowermost level of the *Hipparion* fauna in Yihachi (Zhang et al., 2021) and Guonigou (Fang et al., 2016) is 11.5 Ma, which constrains the upper age limit of the Liushu/Hujialiang Formation. Thus the Liushu/Hujialiang Formation was deposited from 12.8 Ma to 11.6 Ma.

It is hard to define the ages of sediments above the conglomerates since no fossil was found in the Maogou section. The highest sediments could correlate with the "Liushu" Formation by stratigraphic correlation to Yihachi, and a hiatus may exist; N1 may correlate to C5n.2n (with a question mark).

To sum up, the boundaries of these formations are the Liushu/Hujialiang Formation from 12.8 Ma to 11.6 Ma; the Dongxiang Formation deposited between 17.2 Ma and 12.8 Ma; the Shangzhuang Formation from 23 Ma to 17.2 Ma; and the Jiaozigou Formation spanned 29.18 Ma to 23 Ma. Precise ages of the four fossiliferous horizons were thus derived as 11.6 Ma (Zhuanchang), 12.8 Ma (Yangwa), 24–25 Ma (Manshancun), and 29 Ma (Yagou).

6.2. Coevolution of the basin and mammals

The Tala Formation was excluded from this study because of the absence of helpful information on mammal fossils therein. The following section discusses the relationships between sedimentary environments, mammal evolution in the basin, and mammalian adaption to global climate change (Fig. 9).

The Jiaozigou Formation comprises reddish-brown clay/silt clay in its upper 74.5 m. A clear wasp-waist-shaped loop indicates significant quantities of hematite (Fig. 5e), and the IRM acquisition curve shows 63% remanence from a high coercivity component (Fig. 5j and Table 2). The magnetic mineral composition indicates the presence of greater hematite in the sediment. The typical giant rhinos lived in a woodland environment with plenty of high trees, which provided adequate food (leaves and tender twigs or branches). The micromammals from the upper (Mansancun) and basal parts (Yagou) of the Jiaozigou Formation were rodent/lagomorph-dominated faunas. The xerophilous-adapted teeth indicate a relatively arid environment (Wang and Qiu, 2023). To sum up, the Linxia Basin was a semiarid woodland environment in the Late Oligocene (Fig. 9).

AMS projection showed structural stresses along the southwest to the northeast direction in the Jiaozigou Formation; horizontal depositional features in the Shangzhuang Formation (Fig. 6c) indicate tectonic stress from the Tibetan Plateau during the Oligocene in the Linxia Basin. Laji-Maxian Shan in the northern part of the Linxia Basin (Fig. 1) uplifted rapidly at ~22 Ma (apatite (U—Th)/He and fission-track ages) (Lease et al., 2011, 2012), which indicates that the stress from the Tibetan Plateau migrated northward by ~22 Ma. Gypsum, demonstrating a high-salinity arid environment, became the dominant mineral in the Shangzhuang Formation (Fig. 4e and Appendix Fig. 2e). The high-salinity arid environment of the Shangzhuang Formation coincides with Central Asian aridification from 25 to 22 Ma (Guo et al., 2002; Zheng et al., 2015; Zhu et al., 2019).

The "Zebra bed" of the Dongxiang Formation is a typical and recognizable sedimentary sequence and can be found at the center and southern part of the basin. There are fewer greenish-gray clay layers in the southern part than in the center part of the basin, indicating that a vast lake in the basin may have existed during the Middle Miocene. The mineral composition in the reddish-brown clays is similar to that of the Jiaozigou Formation (quartz and carbonate) (Fig. 4), with greater hematite content (Fig. 5 a and b). The greenish-gray layers are dominated by dolomite (Fig. 5), reflecting a salty environment. The interbedded reddish-brown clay/silty clay and greenish-gray clay reflect variations of the depositional environment. Alternating negative/positive oxygen isotopes reflect open/closed (evaporative) lake conditions (Fan et al., 2007), and basin salinity changes. Then, sediment colors roughly reflect environmental changes (reddish-brown/greenish-gray lacustrine sediments represent freshwater/salty water fluctuations). In the revised age model, colorful interbedded sedimentary sequences of the Dongxiang Formation were deposited during the Middle Miocene Climatic Optimum, and the Linxia Basin was under a pan lake environment.

The conglomerates and sandstones of the Liush/Hujialiang Formation contained abundant *Platybelodon* fauna fossils, which were deposited between 12.8 and 11.6 Ma. *Platybelodon* is supposed to have lived near water with plenty of grass, so we assume that the continuous middle Miocene lake in the basin broke up by 12.8 Ma. The uplift of Jishi Shan at 13 Ma (Lease et al., 2011), a nearby regional tectonic activity, might have spread conglomerate and coarse sands in the western part of the Linxia Basin. The provenance investigation revealed more sediments from West Qinling in the Hujialiang Formation than from underlying strata (He et al., 2023). The tectonic activity of Jishi Shan and West Qinling coincided with the disappearance of the vast lake in the basin. Subsequently, water flowed freely in the basin, allowing thick

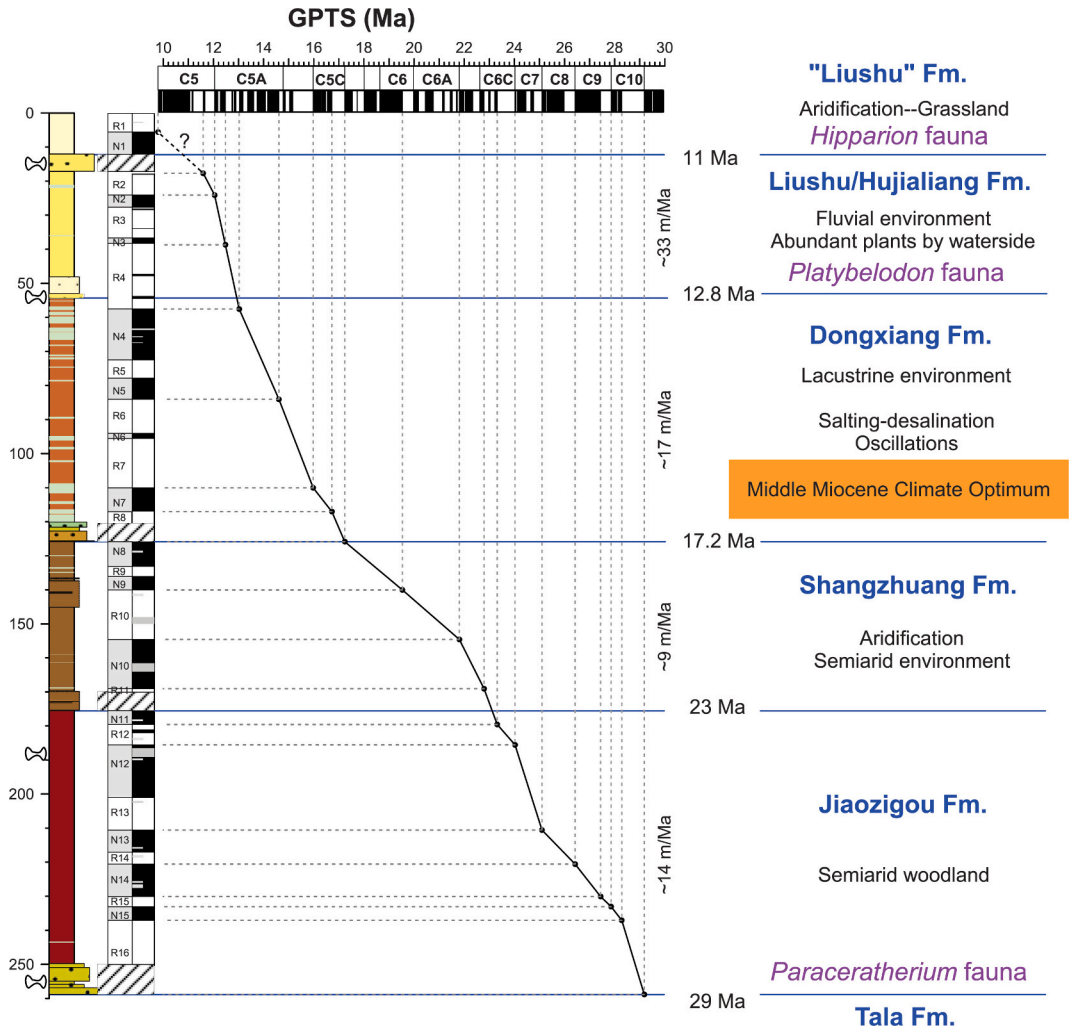

Fig. 9. Age-depth model of the Maogou section and coevolution of basin and mammals.

conglomerates and coarse sands to deposit. The fluvial environment was suitable for *Platybelodon* to thrive.

Hipparion fauna became the predominant mammals since the Late Miocene when steppe and grassland emerged gradually in the basin. Its drier and cooler environment coincides with the cooling trend of the global climate (Zachos et al., 2001). The basin and mammal evolution in the revised age model is strongly related to paleoclimate change and regional tectonic activities.

7. Conclusions

We carried out systematic sedimentological work from 2017 to 2021 to produce stratigraphic correlations from the southern Linxia Basin, rich in mammalian fossils, to the center part, with thick continuous sedimentary sequences. High-resolution paleomagnetic study and micromammal fossil excavation were performed in the Maogou section from the basin's center. The conclusions from our study are as follows.

(1) The Hujialiang Formation bearing *Platybelodon* fauna in the southern part of the Linxia Basin is correlated with the Liushu Formation in the Maogou section in the center part of the basin. The stratum containing *Hipparion* fauna in the basin's southern part is stratigraphically higher and should be renamed "Liushu" Formation, with quotation marks.
(2) A new high-resolution magnetostratigraphic result for the Linxia Basin was established with the constraints of four micromammal fossils. In the new age model, the 259 m sedimentary sequence from the Jiaozigou to the Liushu/Hujialiang formations was deposited between 29 Ma and 11.6 Ma.
(3) *Paraceratherium* fauna occurred at depths between 175 and 259 m (N11-R16), corresponding to chrons C6Cn.3n–C10r, with a duration of ~23–29 Ma; *Platybelodon* fauna occurred at depths between 12 and 54 m (R2-R4), corresponding to chrons C5r.2n–C5Ar.2r, with a duration of ~11.6–12.8 Ma; *Hipparion* fauna is younger than 11.6 Ma.
(4) The Linxia Basin was a semiarid woodland environment during the Late Oligocene and became arid with Asian aridification in the Early Miocene. During the MMCO, a pan lake formed in the basin, and its salinity fluctuated due to climate change. Subsequently, the lake disappeared at ~12.8 Ma due to regional tectonic activities.

Declaration of Competing Interest

The geochronology of the sedimentary sequences in the Linxia Basin has been in great dispute, mainly because the previous magnetostratigraphy was poorly constrained. In this paper, we performed a high-resolution paleomagnetic study and built a revised magnetostratigraphic result with constraints by four micromammal fossil faunas. This new age model would give us new sight into middle Cenozoic tectonic history, paleoclimate, and biological evolution in the northeast border area of the Tibetan Plateau.

The new magnetostratigraphy of our study conflicts with the previous one by Fang et al. (1997, 2003).

Data availability

The data that has been used is confidential.

Acknowledgments

We appreciate help from Chengying LIU, Lu SUN, and Chang LIU in the field and tshe assistance in laboratory work from Dr. Zhongshan SHEN, Shuai ZHANG, and Quan ZENG. Many thanks are given to editors Chenglong DENG and Larry FLYNN and anonymous reviewers for critiquing the manuscript. This work was jointly supported by the Key Project of Frontier Science Research of the Chinese Academy of Sciences (No. QYZDY-SSW-DQC002), National Natural Science Foundation of China (NSFC) (Grant No. 41974079; 41991323), and the National Key R and D project (2022YFF0801502).

Appendix A. Supplementary data

Supplementary data to this article can be found online at https://doi.org/10.1016/j.palaeo.2023.111620.

References

Borradaile, G.J., Jackson, M., 2010. Structural geology, petrofabrics and magnetic fabrics (AMS, AARM, AIRM). J. Struct. Geol. 32 (10), 1519–1551. https://doi.org/10.1016/j.jsg.2009.09.006.

Chen, H., Fang, X., Li, J., Kang, S., 1996. Fission track dating of Cenozoic strata in Linxia Basin. Nuclear Techniques 19 (10), 632–634.

Clark, M.K., Farley, K.A., Zheng, D., Wang, Z., Duvall, A.R., 2010. Early Cenozoic faulting of the northern Tibetan Plateau margin from apatite (U–Th)/He ages. Earth Planet. Sci. Lett. 296 (1–2), 78–88. https://doi.org/10.1016/j.epsl.2010.04.051.

Deng, T., 2004. Establishment of the middle Miocene Hujialiang Formation in the Linxia Basin of Gansu and its features. J. Stratigr. 28 (4), 307–312 (in Chinese with English abstract).

Deng, T., Qiu, Z., Wang, B., Wang, X., Hou, S., 2013. Late Cenozoic Biostratigraphy of the Linxia Basin, Northwestern China. Fossil Mammals of Asia. In: Wang, X., Flynn, L.J., Fortelius, M. (Eds.), Fossil Mammals of Asia. Columbia University Press, New York, pp. 243–273.

Deng, T., Wang, X., Ni, X., Liu, L., Liang, Z., 2004. Cenozoic stratigraphic sequence of the Linxia Basin in Gansu, China and its evidence from mammal fossils. Vertebrata PalAsiatica 42 (1), 45–66.

Egli, R., Chen, A.P., Winklhofer, M., Kodama, K.P., Horng, C.-S., 2010. Detection of noninteracting single domain particles using first-order reversal curve diagrams. Geochem. Geophys. Geosyst. 11 (1) https://doi.org/10.1029/2009gc002916. Q01Z11 (1–22).

Fan, M., Dettman, D.L., Song, C., Fang, X., Garzione, C.N., 2007. Climatic variation in the Linxia basin, NE Tibetan Plateau, from 13.1 to 4.3 Ma: the stable isotope record. Palaeogeogr. Palaeoclimatol. Palaeoecol. 247 (3–4), 313–328. https://doi.org/10.1016/j.palaeo.2006.11.001.

Fang, X., Garzione, C., Van der Voo, R., Li, J., Fan, M., 2003. Flexural subsidence by 29 Ma on the NE edge of Tibet from the magnetostratigraphy of Linxia Basin,China. Earth Planet. Sci. Lett. 210 (3–4), 545–560. https://doi.org/10.1016/s0012-821x(03)00142-0.

Fang, X., Li, J., Wang, J., Zhong, W., Cao, J., et al., 1995. Records of the uplift of the Qinghai-Xizang (Tibetan) Plateau and long-term climate change. In: Uplift of Qinghai-Xizang (Tibet) Plateau and Global Change. Lanzhou University Press, Lanzhou, pp. 19–83. Li et al.

Fang, X., Li, J., Zhu, J., Chen, H., Cao, J., 1997. Absolute age and seperation of Cenozoic strata from the Linxia Basin,Gansu. Chinese Sci. Bull. 42 (14), 1457–1471 (in Chinese).

Fang, X., Wang, J., Zhang, W., Zan, J., Song, C., Yan, M., Appel, E., Zhang, T., Wu, F., Yang, Y., Lu, Y., 2016. Tectonosedimentary evolution model of an intracontinental flexural (foreland) basin for paleoclimatic research. Glob. Planet. Chang. 145, 78–97. https://doi.org/10.1016/j.gloplacha.2016.08.015.

Guo, Z., Ruddiman, W.F., Hao, Q., Wu, H., Qiao, Y., Zhu, R., Peng, S., Wei, J., Yuan, B., Liu, T., 2002. Onset of Asian desertification by 22 Myr ago inferred from loess deposits in China. Nature 416, 159–163.

Harrison, R.J., Feinberg, J.M., 2008. FORCinel: an improved algorithm for calculating first-order reversal curve distributions using locally weighted regression smoothing. Geochem. Geophys. Geosyst. 9 (5) https://doi.org/10.1029/2008GC001987. Q05016 (1–11).

He, M., Zheng, Y., Liu, C., 2023. Cenozoic tectonosedimentary and environmental evolution of the Linxia Basin, NW China, confined by detrital zircon provenance study. Palaeogeogr Palaeoclimatol. Palaeoecol. 10.1016/j.palaeo.2023.111622.

Heslop, D., Dekkers, M.J., Kruiver, P.P., Oorschot, 2002. Analysis of isothermal remanent magnetization acquisition curves using the expectation-maximization algorithm. Geophys. J. Int. 148, 58–64.

Jelinek, V., 1981. Characterization of magnetic fabric of rocks. Tectonophysics 79 (3–4), T63–T67.

Jiang, K., Liang, W., Wu, G., Liu, C., Zou, X., He, X., Li, J., Wang, X., Zheng, B., Shen, Q., 2022. Anisotropy of magnetic susceptibility study and its significance in the late Cretaceous-Cenozoic Sanmenxia Basin in the southeastern Shanxi rift,Central China. Solid Earth Sci. 7 (2), 135–150. https://doi.org/10.1016/j.sesci.2022.02.002.

Lease, R.O., Burbank, D.W., Clark, M.K., Farley, K.A., Zheng, D., Zhang, H., 2011. Middle Miocene reorganization of deformation along the northeastern Tibetan Plateau. Geology 39 (4), 359–362. https://doi.org/10.1130/g31356.1.

Lease, R.O., Burbank, D.W., Hough, B., Wang, Z., Yuan, D., 2012. Pulsed Miocene range growth in northeastern Tibet: insights from Xunhua Basin magnetostratigraphy and provenance. Geol. Soc. Am. Bull. 124 (5–6), 657–677. https://doi.org/10.1130/b30524.1.

Li, J., Fang, X., Zhu, J., Zhong, W., Cao, J.X., Wang, J., Zhang, Y., Wang, J., Kang, S., 1995. Paleomagnetic chronology and type sequence of the cenozoic stratigraphy of the Linxia Basin in Gansu Province of China. Qinghai-Xizang project expert committee. In: Study on the Formation and Evolution of the Qinghai-Xizang Plateau, Environmental Change and Ecological System. Science Press, Beijing, pp. 41–54 (in Chinese with English abstract).

Li, S., van Hinsbergen, D.J.J., Shen, Z., Najman, Y., Deng, C., Zhu, R., 2020. Anisotropy of magnetic susceptibility (AMS) analysis of the Gonjo Basin as an independent constraint to date Tibetan. Geophys. Res. Lett. 47 (8) https://doi.org/10.1029/2020GL087531 e2020GL087531.

Lowrie, W., 1990. Identification of ferromagnetic minerals in a rock by coercivity and unblocking temperature properties. Geophys. Res. Lett. 17 (2), 159–162.

Lurcock, P.C., Wilson, G.S., 2012. PuffinPlot: a versatile, user-friendly program for paleomagnetic analysis. Geochem. Geophys. Geosyst. 13 (6), Q06Z45. https://doi.org/10.1029/2012gc004098.

Ogg, J.G., 2020. Geomagnetic polarity time scale. In: Gradstein, F.M., Ogg, J.G., Schmitz, M.D., Ogg, G.M. (Eds.), Geologic Time Scale 2020. Elsevier, pp. 159–192.

Opdyke, N.D., Channell, J.E.T., 1996. In: Magnetic Stratigraphy. Academic Press, pp. 1–346.

Qin, H., Zhao, X., Liu, S., Paterson, G.A., Jiang, Z., Cai, S., Li, J., Liu, Q., Zhu, R., 2020. An ultra-low magnetic field thermal demagnetizer for high-precision paleomagnetism. Earth Planets Space 72 (1). https://doi.org/10.1186/s40623-020-01304-0, 170 (1–12).

Qiu, Z.X., Xie, J., Yan, D., 1990. Discovery of some early Miocene mammalian fossils from Dongxiang,Gansu. Vertebrata PalAsiatica 28 (1), 9–24.

Qiu, Z.X., Qiu, Z.D., Zheng, Y., Li, L., 2023. Historical review of stratigraphic study of Oligocene-Pliocene mammal-fossil bearing deposits in Linxia Basin, Gansu Province, and the current controversies. Palaeogeogr. Palaeoclimatol. Palaeoecol. under review.

Qiu, Z., Wang, B., Deng, T., 2004. Indricotheres (perissodactyla,mammalia) from Oligocene in linxia basin, Gansu, China. Vertebrata PalAsiatica 42 (3), 177–192.

Qiu, Z.D., Wang, B.Y., Li, L., 2023. Middle Cenozoic micromammals from Linxia Basin, Gansu Province, China, and their implications for biostratigraphy and palaeoecology. Palaeogeogr. Palaeoclimatol. Palaeoecol. 616, 11467.

Qiu, Z.X., Wang, B.Y., Deng, T., 2004. Mammal fossils from Yagou, Linxia Basin, Gansu, and related stratigraphic problems. Vertebrata PalAsiatica 42 (4), 276–296.

Roberts, A.P., Pike, C.R., Verosub, K.L., 2000. First-order reversal curve diagrams: a new tool for characterizing the magnetic properties of natural samples. J.Geophys.Res. Solid Earth 105 (B12), 28461–28475. https://doi.org/10.1029/2000jb900326.

Staisch, L.M., Niemi, N.A., Clark, M.K., Chang, H., 2020. The cenozoic evolution of crustal shortening and left-lateral shear in the Central East Kunlun Shan: implications for the uplift history of the Tibetan Plateau. Tectonics 39 (9). https://doi.org/10.1029/2020tc006065.

Sun, L., Deng, C., Deng, T., Kong, Y., Wu, B., Liu, S., Li, Q., Liu, G., 2023. Magnetostratigraphy of the Oligocene and Miocene of the Linxia Basin, northwestern China. Palaeogeogr. Palaeoclimatol. Palaeoecol. 613, 111404 https://doi.org/10.1016/j.palaeo.2023.111404.

van Hinsbergen, D.J., Lippert, P.C., Dupont-Nivet, G., McQuarrie, N., Doubrovine, P.V., Spakman, W., Torsvik, T.H., 2012. Greater India Basin hypothesis and a two-stage Cenozoic collision between India and Asia. Proc. Nat. Acad. Sci. 109 (20), 7659–7664. https://doi.org/10.1073/pnas.1117262109.

Wang, B.Y., Qiu, Z.X., 2023. Micromammal Fossils from the basal part of the Jiaozigou Formation in Yagou area, Linxia Basin, Gansu Province. Palaeogeogr. Palaeoclimatol. Palaeoecol. in press.

Wang, B.Y., Qiu, Z.X., Wang, S., 2023. Mansancun micromammal fauna from the upper part of the Jiaozigou Formationin Linxia Basin, Gansu Province. Vertebrata PalAsiatica 61 (1). https://doi.org/10.19615/j.cnki.2096-9899.2212xx.

Xiao, R., Zheng, Y., Liu, X., Yang, Q., Liu, G., Xia, L., Bian, Z., Guan, J., Feng, P., Xu, H., Clift, P.D., Qiang, X., Zhang, Y., Zheng, H., 2021. Synchronous Sedimentation in Gonjo Basin, Southeast Tibet in Response to India-Asia Collision Constrained by Magnetostratigraphy. Geochem. Geophys. Geosyst. 22 (3) https://doi.org/10.1029/2020gc009411 e2020GC009411 (1–22).

Zachos, J., Pagani, M., Sloan, L., Thomas, E., Billups, K., 2001. Trends, Rhythms, and aberrations in global climate 65 Ma to present. Science 292 (5517), 686–693. https://doi.org/10.1126/science.1059412.

Zhang, W., Erwin, A., Wang, J., Fang, X., Zan, J., Yang, Y., Miao, Y., Yan, X., 2019. New paleomagnetic constraints for Platybelodon and Hipparion faunas in the Linxia Basin and their ecological environmental implications. Global Planet. Change 176, 71–83. https://doi.org/10.1016/j.gloplacha.2019.03.002.

Zhang, R., Wei, X., Kravchinsky, V.A., Yue, L., Zheng, Y., Qin, J., Yang, L., Ma, M., Xian, F., Gong, H., Zhang, Y., Liu, X., 2021. "Tiny Wiggles" in the Late Miocene Red Clay Deposits in the North-East of the Tibetan Plateau. Geophys. Res. Lett. 48 (16) https://doi.org/10.1029/2021gl093962 e2021GL093962 (1–11).

Zheng, H., Wei, X., Tada, R., Clift, P.D., Wang, B., Jourdan, F., Wang, P., He, M., 2015. Late Oligocene-early Miocene birth of the Taklimakan Desert. Proc. Natl. Acad. Sci. U. S. A. 112 (25), 7662–7667. https://doi.org/10.1073/pnas.1424487112.

Zhu, C., Meng, J., Hu, Y., Wang, C., Zhang, J., 2019. East-Central Asian climate evolved with the northward migration of the High Proto-Tibetan Plateau. Geophys. Res. Lett. 46 (14), 8397–8406. https://doi.org/10.1029/2019gl082703.